IRAMP
13(1), Jan 2022, pp. 15-25

ISSN: 2229-39-44

Features of Hydroxyl Emission Spectroscopy in Laboratory-Air Laser-Plasma

CHRISTIAN G. PARIGGER

Physics and Astronomy Department, University of Tennessee, University of Tennessee Space Institute, Center for Laser Applications, 411 B.H. Goethert Parkway, Tullahoma, TN 37388-9700, USA; cparigge@tennessee.edu

ABSTRACT: This work presents experimental results of spatiotemporal diagnosis of hydroxyl, OH, in laser- plasma in laboratory air at standard ambient temperature and pressure. Measured shadowgraph sequences of laser-induced optical breakdown reveal the extent of correlations with recorded diatomic spectra. Optical breakdown plasma is initiated using near-ir radiation from a standard Q-switched laser device that is capable of providing 6 nanosecond, 850 milli Joule pulses at a wavelength of 1064 nanometer, and focal irradiance in the range of 1 to 10 Tera Watt/cm^2. Frequency doubled beams are utilized for capturing shadowgraphs for visualization of the breakdown kernel at time delays in the range of 0.1 to 100 microsecond. Emission spectra of the laser plasma, spatially resolved along the slit dimension, are recorded in the wavelength range of 300 nm to 322 nm, and with gate widths adjusted to 10 microsecond for the intensified charge-coupled device that is mounted at the exit plane of a 0.64 m Czerny-Turner configuration spectrometer. For time delays larger than 20 microsecond, integrated molecular OH signals occur due to recombination of the plasma. In addition, discussion is included regarding molecular spectra of N_2, CN, and presence of atomic spectra in the laser plasma.

Keywords: Molecular Spectroscopy; Diatomic Molecules; Optical Emission Spectroscopy; Laser Induced Optical Breakdown; Hydroxyl; Nitrogen Second Positive; Cynaide; Atomic Spectroscopy; Plasma Physics;

1. INTRODUCTION

Plasma emission spectroscopy of hydroxyl (OH) diatomic molecules shows a volley of diagnosis applications in plasma physics and analytical chemistry, and obviously, in combustion physics and chemistry [1–4]. This work initiates laser-plasma [5–8] in standard ambient temperature (SATP) and pressure laboratory air. The primary reason for occurrence of OH is the presence of moisture in SATP air, however, OH emission signals show spectroscopic interference from the N_2 Second Positive system that usually occurs in nitro- gen discharges [9]. Recorded spectra in air breakdown dwarf signal strengths that can be measured in combustion processes that utilize oxygen as oxidizer, for example, combustion of hydrocarbons [10, 11]. However, when exploring combustion and laser-plasma in gases, usually strong signals define the spectroscopy of emanating light with notable contributions of diatomic carbon (C2) Swan bands, cyanide (CN), and atomic signatures of the hydrogen Balmer series, e.g., hydrogen-beta line [12–16]. Laser-plasma in air, and for the wavelength range of 300 nm to 320 nm, reveals significant contributions from the N_2 Second Positive system of nitrogen at time delays of typically 20 microsecond after optical breakdown [17], and OH emission signals are clearly discernable in the time delay range of 50 µs to 110 µs. Spatiotemporal information is obtained by utilizing the slit dimension for the spatial resolution. The temporal resolution is obtained from a systematic set of time delays that are selected for an intensified charge-coupled device (iCCD) mounted at the exit plane of a spectrometer. The experimental methodology including choice of laser-plasma generation by aligning beam propagation and focusing parallel to the slit is analogous to that designed for recent cyanide, CN, diatomic molecular studies [18]. The shadowgraphs are recorded by employing a digital camera, thereby allowing one to associate spatial connections with the time-resolved, recorded spectra. The average concentration of OH molecules is inferred from equilibrium species distributions computations that employ freely available code for chemical equilibrium with applications [19, 20].

2. EXPERIMENTAL DETAILS

The experimental arrangement for recording of spatiotemporal molecular distributions has been communicated previously, however, for completeness is included in this work. The standard experimental components are used for laser-induced breakdown spectroscopy and have been summarized previously, e.g., see Ref. [17].

The experimental arrangement consists of a set of components typical for time-resolved, laser-induced optical emission spectroscopy, or nanosecond laser-induced breakdown spectroscopy (LIBS). Primary instrumentations include a Q-switched Nd:YAG device, Quantel model Q-smart 850, operated at the fundamental wavelength of 1064-nm to produce full-width-at-half-maximum 6-ns laser radiation with an energy of 850 mJ per pulse, a laboratory type Czerny-Turner spectrometer, Jobin Yvon model HR 640, with a 0.64 m focal length and equipped with a 1200 grooves/mm grating, an intensified charge-coupled device, Andor Technology model iStar DH334T-25U-03, for recording of temporally and spatially resolved spectral data, a laboratory chamber or cell with inlet and outlet ports together with a vacuum system, electronic components for synchronization, and various optical elements for beam shaping, steering and focusing. Figure 1 displays the principal schematic of the experimental arrangement. For 1:1 imaging of the plasma onto the 100 µm spectrometer slit, a fused silica plano-convex lens, Thorlabs model LA4545, is employed. For the OH experiments, the laser pulse energy is attenuated with beam splitters and apertures from 850 to 170 mJ/pulse. The laser beam is focused at the same position as for experiments in a chamber, but for the reported OH measurements the cell in Fig. 1 was removed.

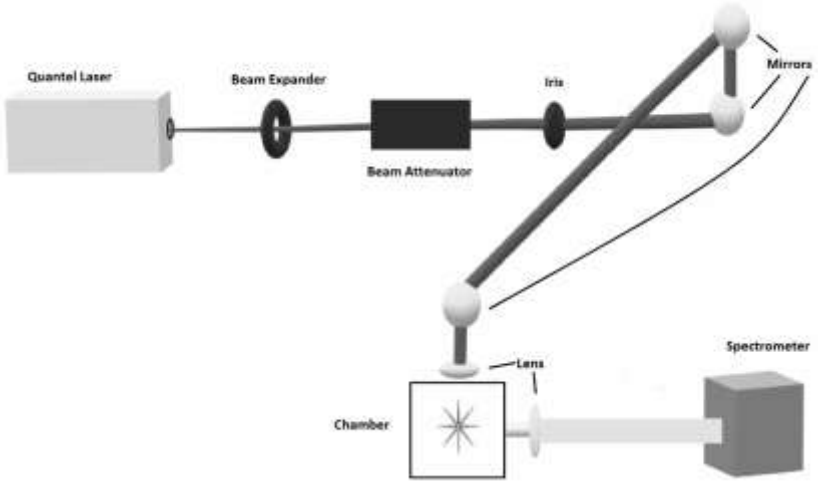

Fig. 1. Experimental arrangement for laser-induced breakdown spectroscopy

For visualization studies reported here, two separate laser device, Continuum Surelite model SL I-10, were frequency-doubled to operate at the 2nd harmonic, 532-nm wavelength, and both breakdown and shadowgraph beams are spatially overlapped. The shadowgraph pulses can be delivered with a minimum time delay of 300 ns and with a well defined time delay shown in less than ±1 ns trigger-jitter between the pulses. Shadowgraphs are recorded by external synchronization of the Surelite and Quantel laser devices and by externally triggering the camera, Silicon Video 9C10 color camera, that records the images that are projected onto a screen. Figure 2 illustrates the modular setup for recording shadowgraphs.

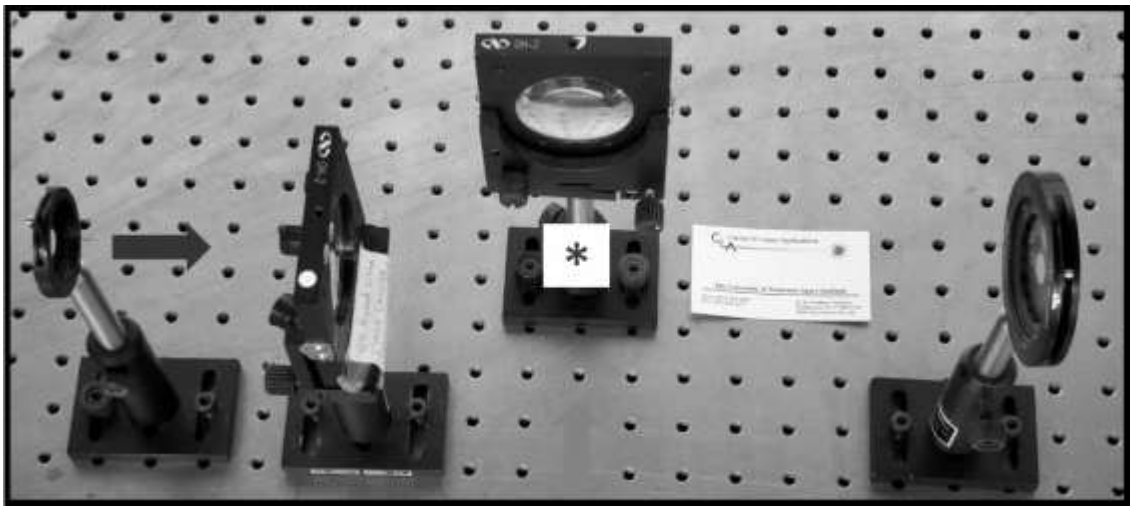

Fig. 2. Module for recording shadowgraphs of optical breakdown in air. The collimated laser beam (horizontal arrow) is focused with f/20 optics. The asterisk symbolically indicates optical breakdown. The interaction area is illuminated by a time-delayed laser beam (vertical arrow at center bottom of the image), and shadows are projected onto a screen (not shown) and recorded with a digital camera [17].

In studies with time-resolved spectroscopy, optical breakdown was generated at a rate of 10 Hz, with the laser beam focused with f/5 optics from the top, or parallel to the slit, analogous to recently reported CN laser spectroscopy [18]. Figure 3 illustrates the experimental arrangement for imaging of the laser-plasma onto the vertical slit of the spectrometer. The laser beam, parallel to the slit, arrives from the top (vertical arrow) and is focused with f/5-optics by an anti-reflection coated, 25.4-mm (1 in.) lens. The air-breakdown plasma, indicated by the asterisk is imaged 1:1 with a 50.8-mm lens.

In the experiments, the irradiance is of the order of 10× more than that needed for optical breakdown in dry air. The detector pixels are grouped together in 4-pixel tracks along the slit direction, resulting in obtaining 256 spectra for each time delay. Measurements comprise

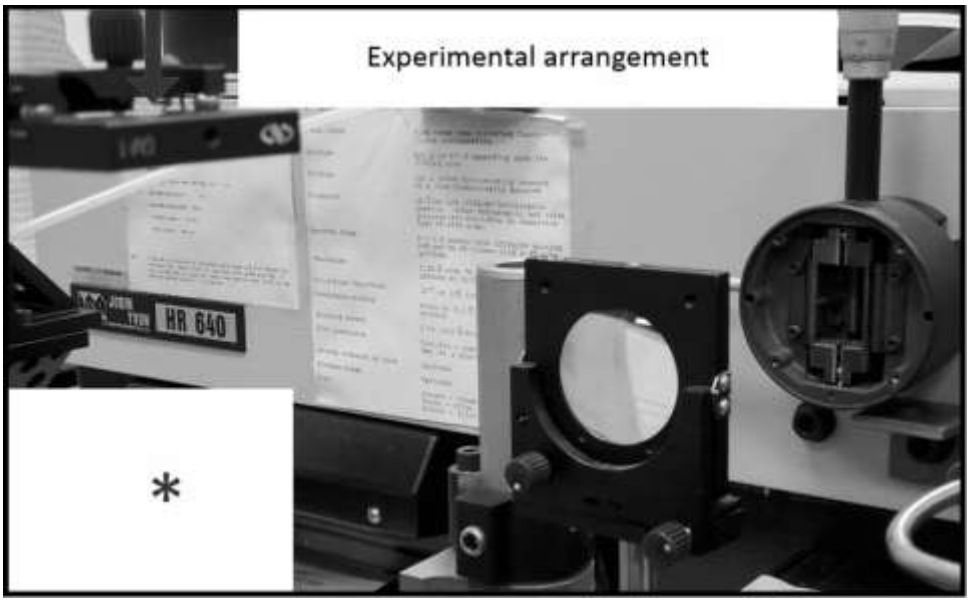

Fig. 3. Experimental arrangement for time-resolved spectroscopy. The laser beam (vertical arrow) is focused to generate optical breakdown, indicated by the asterisk in the lower left of the photograph. The plasma is 1:1 images onto the slit of the spectrometer. Time-resolved data are recorded with an intensified charge-coupled device (not shown) positioned at the exit plane of the spectrometer [17].

accumulation of 100 consecutive laser-plasma events for 11 separate time delays at 10 μs steps with a 10 μs gate centered at the selected time delay. The selected series explores the plasma decay with specific attention to recognition of OH molecular data that are free from spectroscopic interference. However, the 0-0 OH band edge is recognizable for time delays of about 20 μs, but almost N_2 interference-free data are captured for time delays as early as about 50 μs.

3. RESULTS AND DISCUSSION

A. Computation of Hydroxyl Spectra

Computation of hydroxyl spectra utilizes well-established line-strength data for the diatomic OH molecule. Application of standard quantum mechanics establishes within the concept of line strengths [21] consistent computation of diatomic spectra. The OH line-strength data are published as a supplement to a recent paper on hydroxyl [17].

Figure 4 illustrates computed OH data for spectral resolutions of 0.25 nm and 0.0025 nm that correspond to typical resolutions in laser-induced spectroscopy with intensified array detectors and nominal pico-meter resolution stick-spectra. OH spectra in the indicated 300 nm to 330 nm wavelength range clearly show the 0-0 band edge near 306 nm of the red shaded A $^2\Sigma^+ \leftrightarrow$ X $^2\Pi_i$ ultraviolet system, the 1-1 band edge is near 312 nm, and the 2-2 band edge near 318 nm [17].

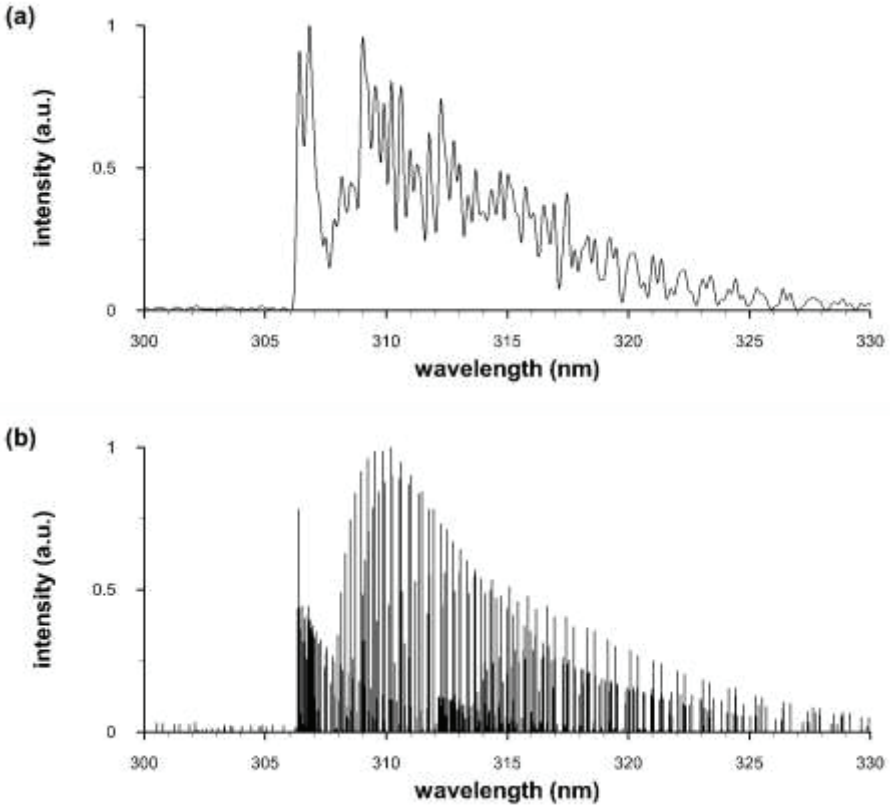

Fig. 4. Computed spectra: T = 6,000 K; Spectral resolution (a) 0.25 nm and (b) 0.0025 nm [17].

The calculation of the spectra relies on the use of OH line strength data [17]. Computation of diatomic spectra utilizes high resolution data for determination of molecular constants of selected molecular transitions from an upper to a lower energy level. Numerical solution of the Schrödinger equation for potentials yield r-centroids associated with vibrational transitions, viz. Frank-Condon factors. Calculated rotational factors are interpreted as selection rules because these factors are zero for forbidden transitions, viz. Hönl-London factors.

B. Shadowgraphs

Investigations of expanding laser-induced shockwaves and fluid-physics phenomena utilize effectively high shutter-speed shadowgraph photography. Figure 5 displays early time delay, 1 μs and superimposed 0.1 μs, images.

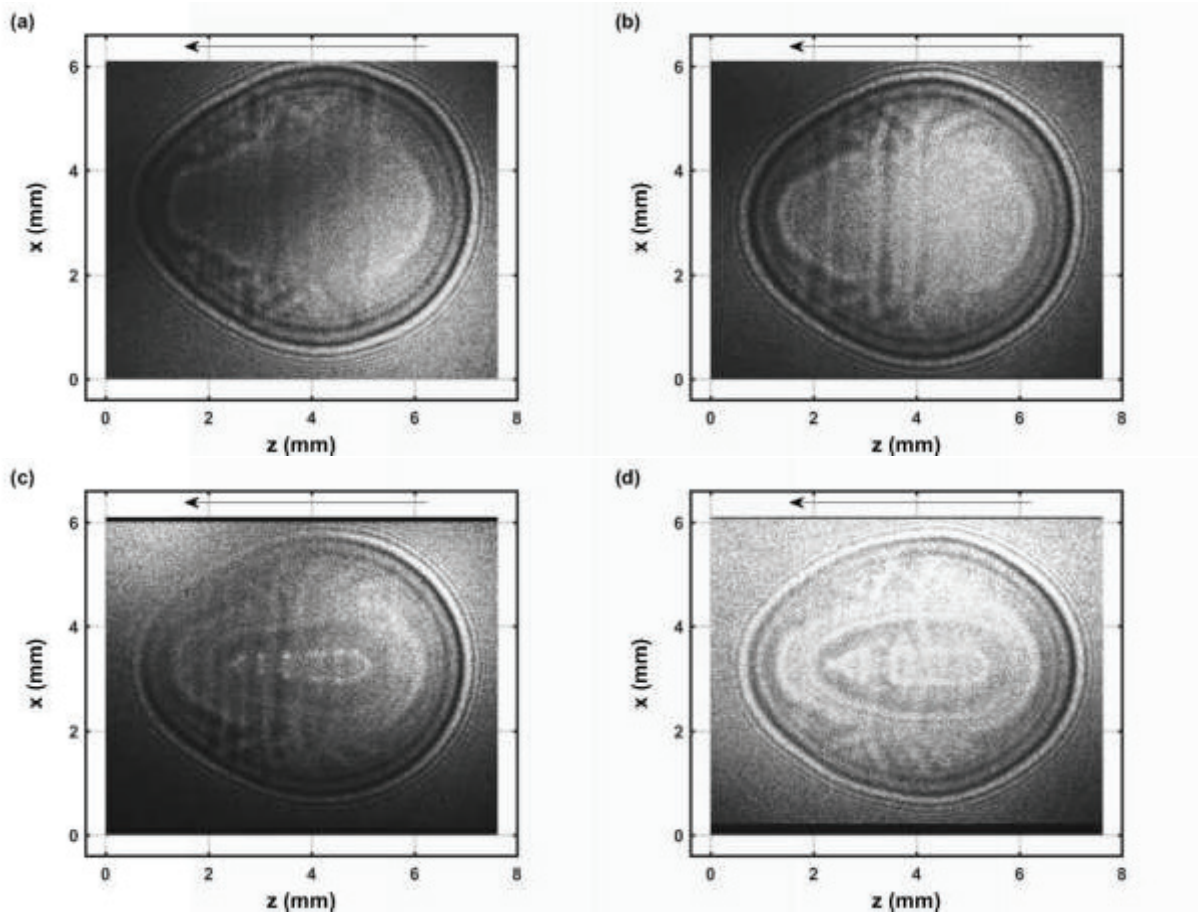

Fig. 5. Single-shot shadowgraph of the expanding laser-induced plasma initiated with a 170-mJ, 6-ns, 1064-nm focused beam, and imaged using a 5-ns, 532-nm back-light that is time-delayed by 1 μs (a) and (b). Double images for time delays of 1 μs and 0.1 μs (c) and (d).

The ir laser beam is focused from right to left as indicated by the arrow in the images. The shock wave appears nearly symmetrical for the 1 μs images that evolved from a spheroidal image captured for time delays of 0.1 μs. In the 0.1 to 1 μs range, CN recombination spectra are measured [18]. The species density increase of electrons and diatomic molecular CN near the shockwave can be determined using Abel integral inversion [18].

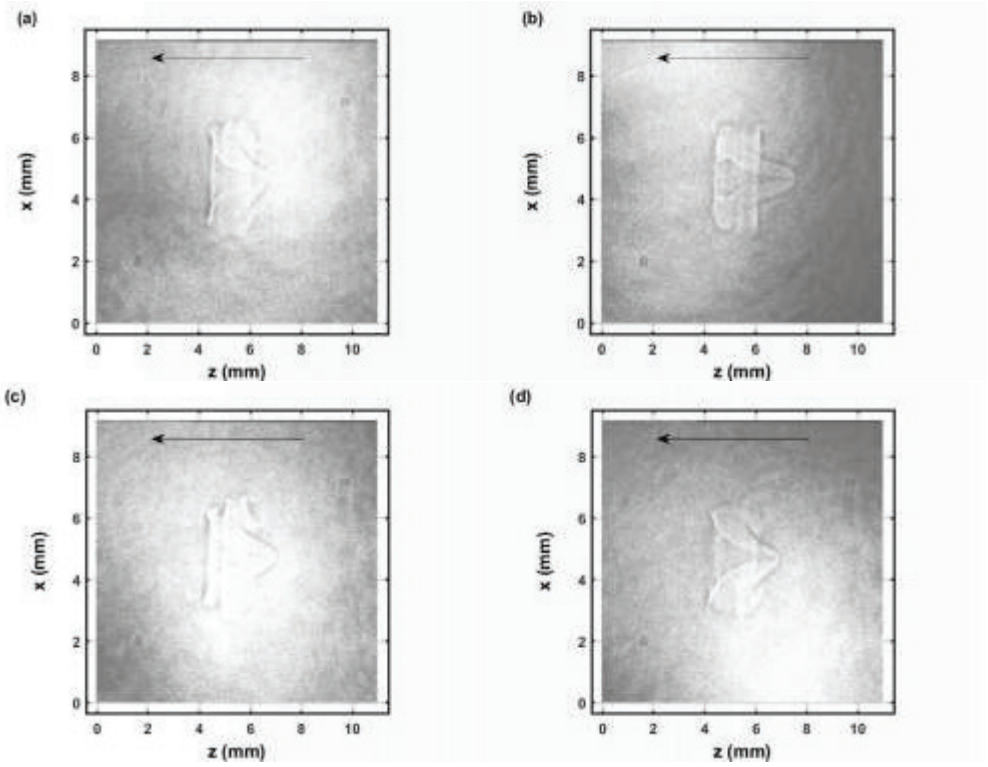

Fig. 6. Single-shot shadowgraph of the expanding laser-induced plasma initiated with a 170-mJ, 6-ns, 1064-nm focused beam, and imaged using a 5-ns, 532-nm back-light that is time-delayed by 54.25 μs (a),(b),(c), and (d) display images from separate laser pulses.

Figures 6 and 7 illustrate selected shadowgraphs for time delays of 54.25 μs and 104.25 μs, respectively. Well developed vortices and fluid flow appear towards the incoming laser beam. The captured images for 54.25-μs time delays (Fig. 6) appear to show slightly more apparent variations than those for 104.25-μs time delays (Fig. 7). However, spatial variations are not obvious in the measured spatiotemporal OH spectra that are communicated in the next section.

In view of laser spectroscopy, time-resolved data taken along a narrow slice along the direction of the laser beam would be affected by fluid dynamics. By comparison, Fig. 5 indicates close to spherical symmetry allowing one to utilize Abel inverse transform algorithms [18]. Spectroscopic diagnosis and correlation with the shadowgraphs of Figs. 6 and 7 is ex-

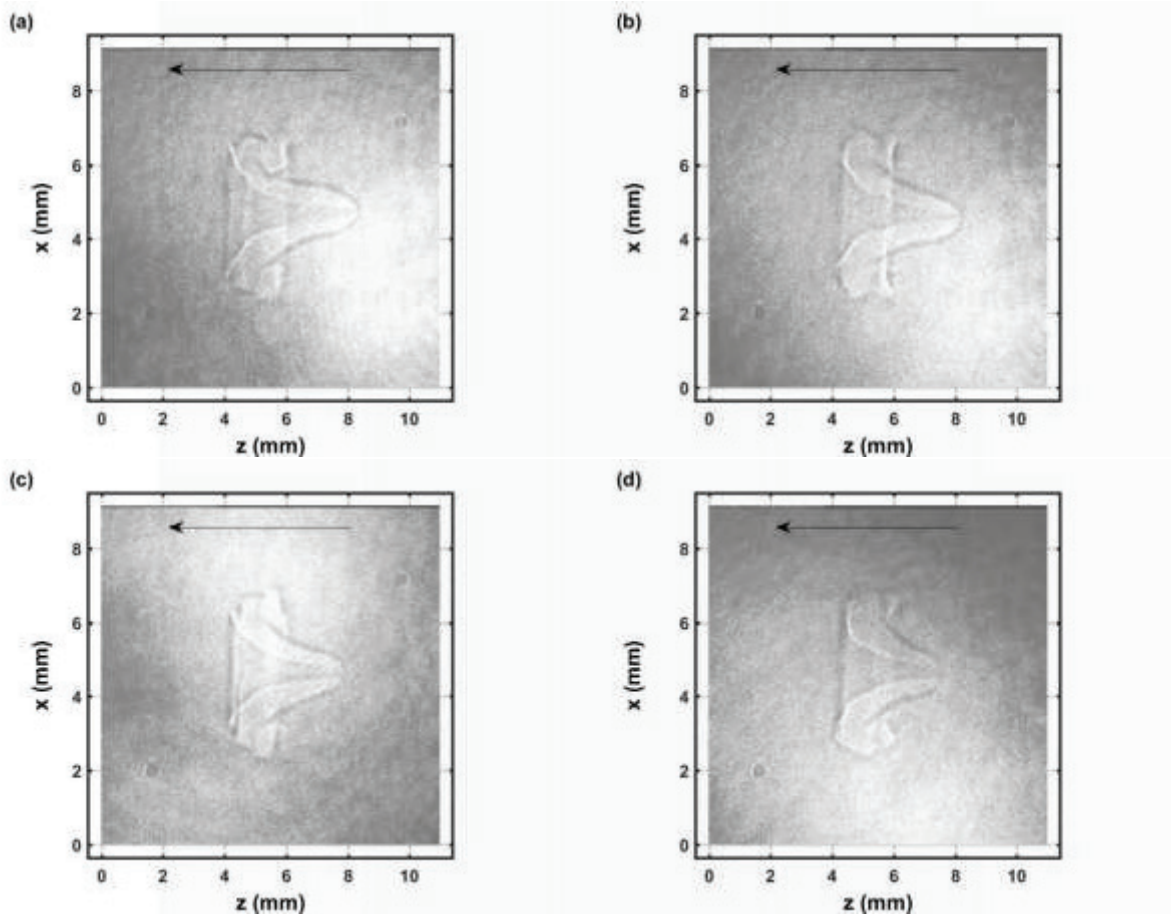

Fig. 7. Single-shot shadowgraph of the expanding laser-induced plasma initiated with a 170-mJ, 6-ns, 1064-nm focused beam, and imaged using a 5-ns, 532-nm back-light that is time-delayed by 104.25 μs (a),(b),(c), and (d) display images from separate laser pulses.

pected to require simultaneous measurements in multiple or at least two directions, in other words, desirable is a computed tomography approach that utilizes Radon inverse transform. For the employed experimental arrangement, line-of-sight integration occurs along the slit-height causing ambiguities in inferences of densities for obviously non-spherical expansion. However, the overall fluid expansion has been measured and computed previously in combustion research along with experimental studies utilizing planar laser-induced fluorescence [10, 11].

C. Emission Spectra

Figures 8, 9, and 10 illustrate recorded emission spectra along the slit height and in the range of 302 nm to 321.3 nm, and for time delays of 10 to 110 μs in 10μs steps. All images are individually scaled from minimum to maximum and processed for grey-scale display.

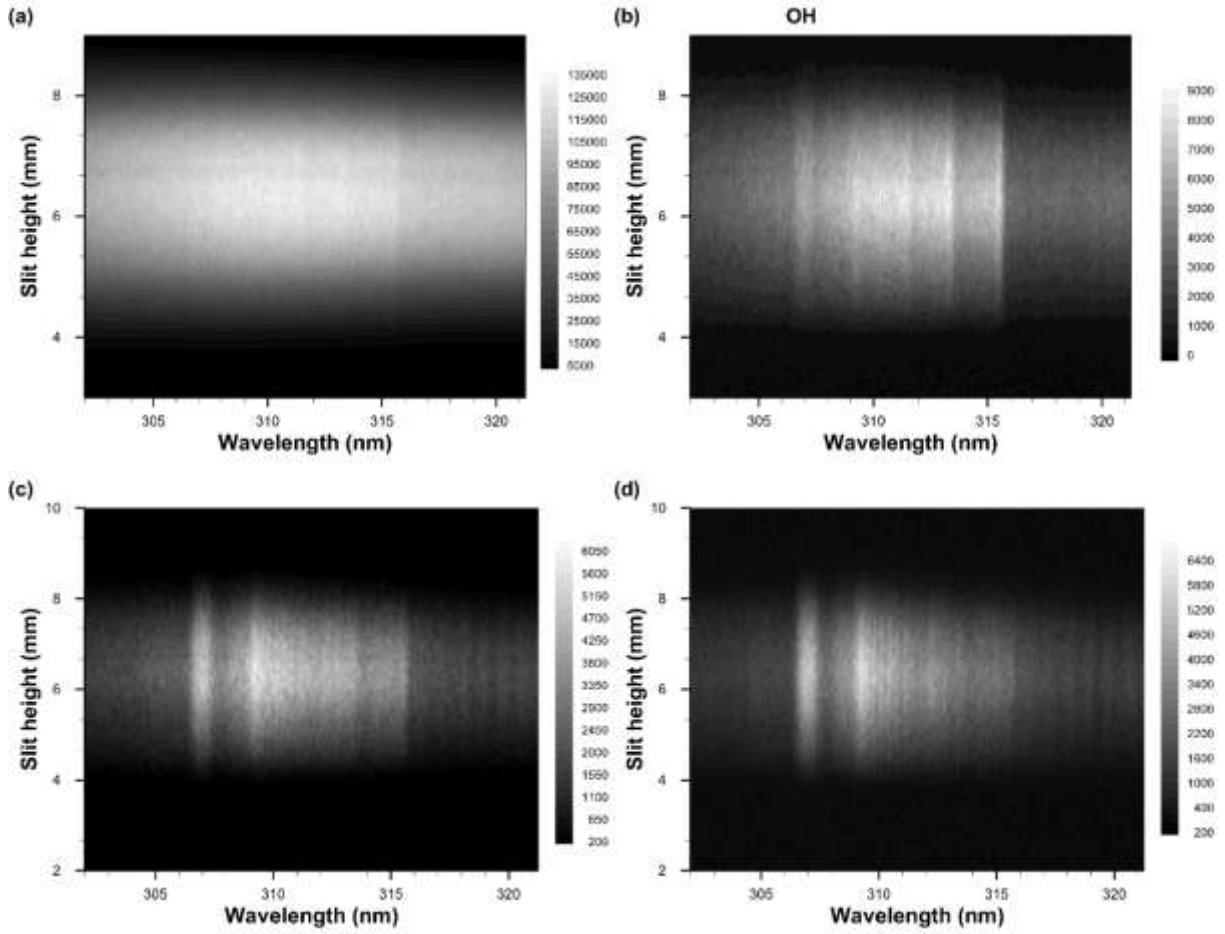

Fig. 8. Recorded data of slit-height vs. wavelength. Gate width: 10 μs, time delay (a) 10 μs – primarily N_2 second positive spectra, (b) 20 μs, (c) 30 μs, and (d) 40 μs. The A-X 0-0 band edge is identified in figure (b). Each grey-scale displayed image is scaled from minimum to maximum.

Fig. 10 (d) displays an average spectrum at 110-μs time delay. The intensified detector has the capability of recording 1024 spatially resolved data, however, 4 vertical pixels are grouped together for increased sensitivity of the actually recorded 256 spectra. The figures illustrate reasonable integrated signals from 100 consecutive laser-plasma events that are dispersed in approximately 100 spectra in the central region of the detector. Fig. 8 (a) displays faint N_2 Second Positive band-edge signals near 315 nm, but Fig. 8 (b) reveals the OH A-X 0-0 band edge near 306 nm together with well demarcated N_2 signals. Figs. 8 (c) and (d) depict how N_2 signals diminish as OH becomes apparent.

Experimental averaging over 100 consecutive laser-plasma events enhances the signal to noise ratio by one order of magnitude. Conversely, as one collapses the 1024 vertical pixels to a single super-pixel, one mimics a linear diode array capable of recording single-shot OH spectra in laboratory air. Inspection of the spectra reveals that there is a slight curvature that would cause decreased resolution when averaging the central spectra.

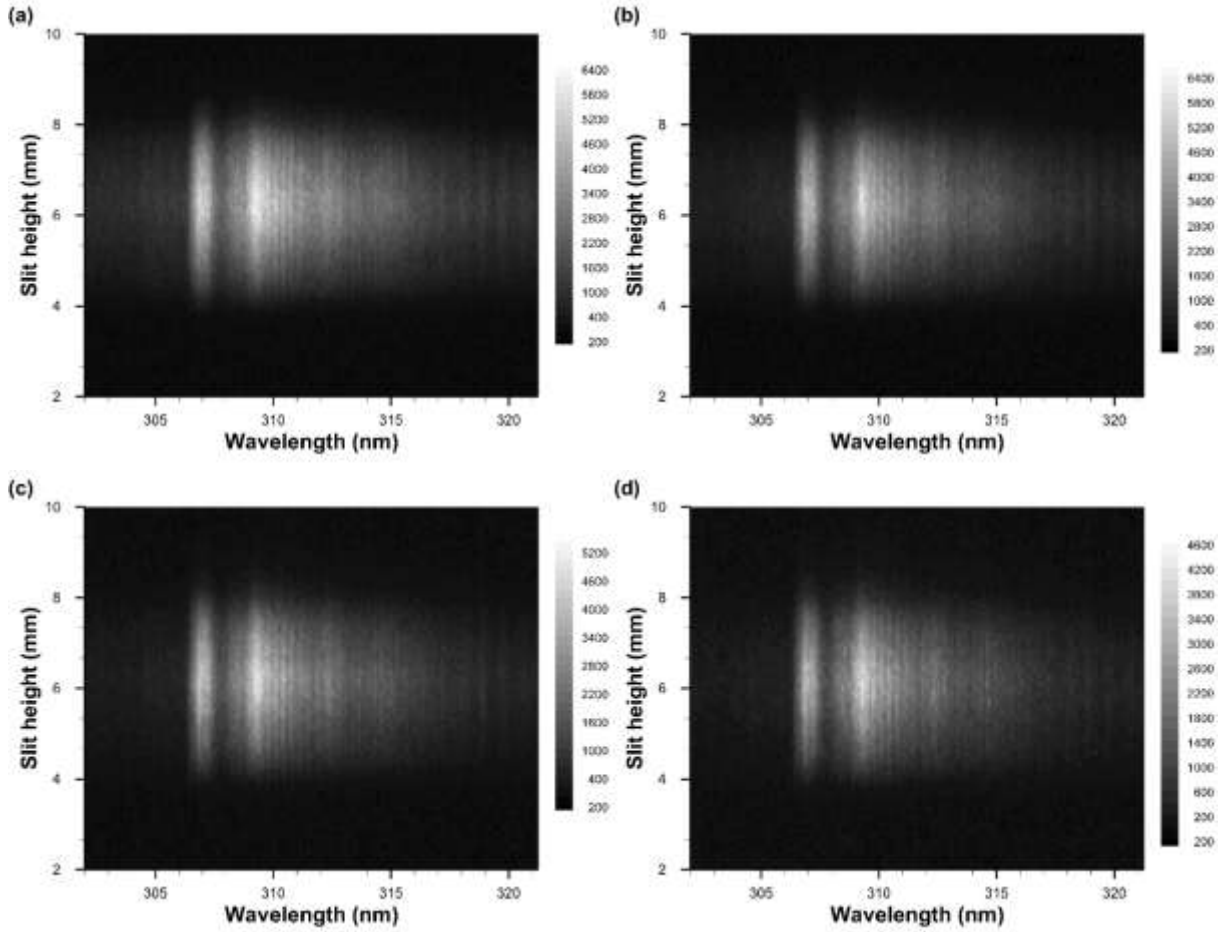

Fig. 9. Recorded data of slit-height vs. wavelength. Gate width: 10 µs, time delay (a) 50 µs primarily OH spectra, (b) 60 µs, (c) 70 µs, and (d) 80 µs. Each grey-scale displayed image is scaled from minimum to maximum.

Figures 9 (a) and (b) indicate similar, OH-band integrated signals or close to maximum OH signals as function of temperature if one computes the equilibrium species density v. temperature [17] and for a measured level of humidity. For air with 25% relative humidity, the OH density reaches a maximum of $\simeq 3 \times 10^{16}\,\mathrm{cm}^{-3}$ at a temperature of $T \simeq 3100\,\mathrm{K}$.

Figure 10 illustrates the persistence of OH emission spectra for time delays of 90 µs to 110 µs, including two resolved peaks near the A-X 0-0 OH band edge that can be seen for an experimental spectral resolution of 0.25 nm. Figure 10(d) indicates the extracted average signal for the central region of the 110-µs time-delay data. Measurement of OH in Moisture-laden laboratory air can be accomplished at the single-shot level as elaborated above, i.e., when grouping together all vertical bins, thereby simulating a linear diode array.

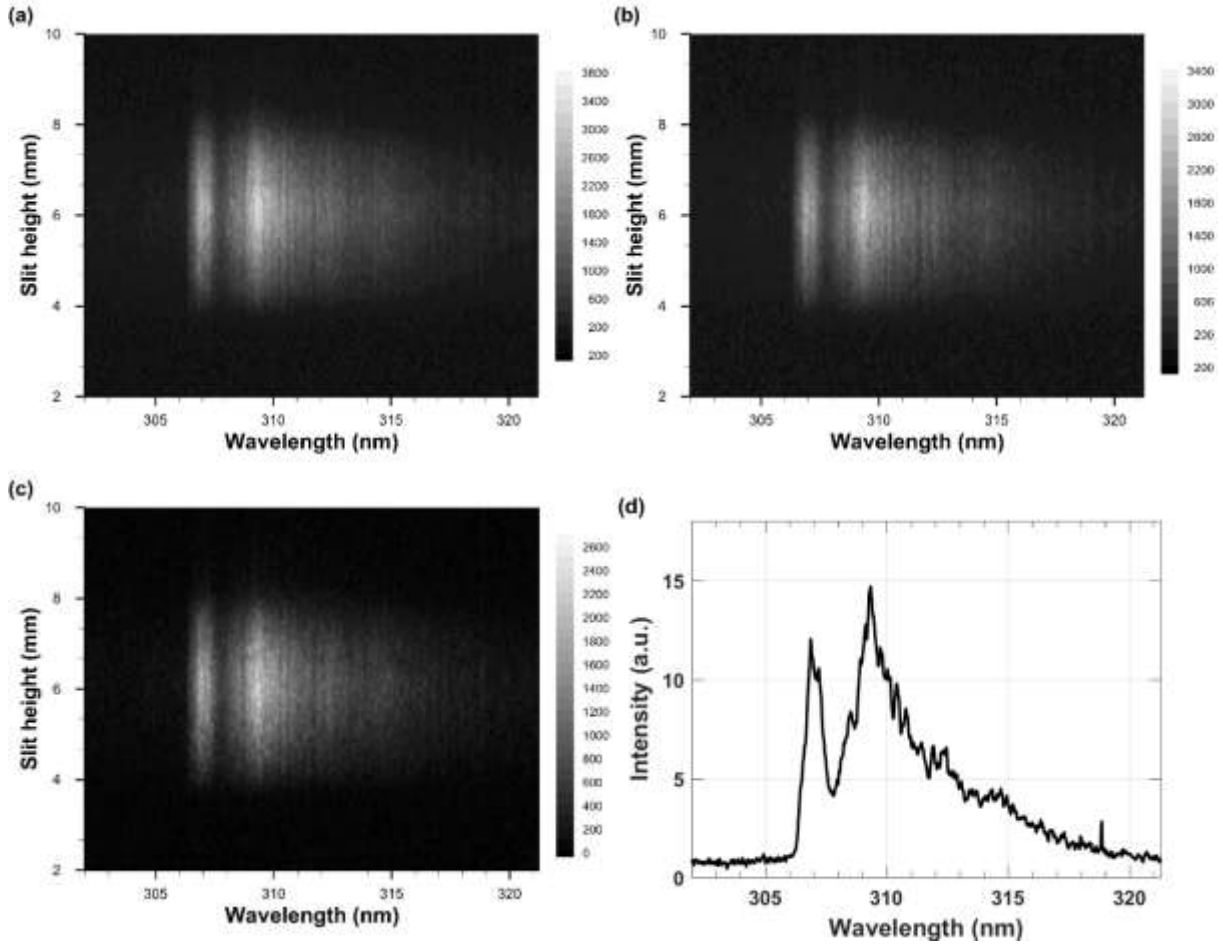

Fig. 10. Recorded data of slit-height vs. wavelength. Gate width: 10 µs, time delay (a) 90 µs primarily OH spectra, (b) 100 µs, (c) 110 µs, and (d) average OH spectra for 110 µs. Each grey-scale displayed image is scaled from minimum to maximum.

In combustion investigation of for example hydrocarbon laser ignition, OH signals are significantly larger than those obtained in laboratory air breakdown. However, planar laser induced fluorescence, or planar LIF, is usually applied in laser-initiated combustion that allows one to correlate shadowgraphs with fluid physics expansion of the kernel [10, 11]. The recorded optical emission data of OH are difficult to connect with the measured shadowgraphs [17]. However, spectra of CN that are recorded within the first microsecond after initiation of laser plasma in laboratory can be associated with the expanding shock wave [18]. An increase in electron density is inferred near the shockwave from analysis of a car- bon atomic line superposed with the CN emission spectrum, and Abel inversion techniques allows one to associate increased CN density near the expanding shock wave.

4. CONCLUSIONS

A correlation of spatially- and temporally- resolved OH emission spectra and of shadowgraphs is difficult. OH signals are clearly discernible at time delays of typically 50 microsecond after plasma initiation. For such time delays, fluid physics phenomena become apparent and appear cylindrically symmetric, but the laser-plasma kernel can not be modeled as spherically symmetry. For time delays of 1 microsecond, the shock wave appears spherically symmetric allowing one to utilize Abel inverse integral techniques to determine the spatial electron density and diatomic molecular CN distribution. However, when utilizing chemical equilibrium distribution predictions for moisture laden air, one can infer OH concentrations in laboratory air breakdown.

ACKNOWLEDGMENTS

The author acknowledges support in part by the State of Tennessee funded Center for Laser Applications at the University of Tennessee Space Institute.

References

[1] Kunze, H.-J. Introduction to Plasma Spectroscopy, Springer, Heidelberg, GER, 2009.

[2] Fujimoto, T. Plasma Spectroscopy, Clarendon Press, Oxford, UK, 2004.

[3] Ochkin, V.N. Spectroscopy of Low Temperature Plasma, Wiley-VCH, Weinheim, GER, 2009.

[4] Boulos, M.I.; Fauchais, P.; Pfender E. Thermal Plasmas. Fundamentals and Applications, Plenum Press, London, UK, 1994.

[5] Radziemski, L.J.; Cremers, D. A., Eds. Laser-Induced Plasmas and Applications, Dekker: New York, NY, USA, 1989.

[6] Miziolek, A.W., Palleschi, V., Schechter, I., Eds. Laser Induced Breakdown Spectroscopy (LIBS): Fundamentals and Applications, Cambridge Univ. Press: New York, NY, USA, 2006.

[7] J.P. Singh; S.N. Thakur, Eds. Molecular Laser-Induced Breakdown Spectroscopy, Laser Induced Breakdown Spectroscopy, 2nd Ed., Elsevier: New York, Amsterdam, NL, 2020.

[8] De Giacomo, A.; Hermann, J. *J. Phys. D: Appl. Phys* 2017, *50*, 183002, 17 pp.

[9] Fatima, H.; Ullah, M. U.; Ahmad, S.; Imran, M.; Sajjad, S.; Hussain, S.; Qayyum, A. *SN Applied Sciences 3*, 2021, 646, 12 pp.

[10] Chen Y.-L.; Lewis, J.W.L. *Opt. Express* 2001, *9*, 360–372.

[11] Qin, W.; Chen, Y.-L.; Lewis, J.W.L. *International Flame Research Foundation (IFRF)* Combust. *J.* 2005, *ISSN: 1562-479X*, 200508.

[12] Parigger, C.G. Laser-induced breakdown in gases: Experiments and simulation. In *Laser Induced Breakdown Spectroscopy (LIBS): Fundamentals and Applications*; Miziolek, A.W., Palleschi, V., Schechter, I., Eds.; Cambridge Univ. Press: New York, NY, USA, 2006; Chap. 4, pp. 171–193.

[13] Parigger, C.G.; Surmick, D.M.; Helstern, C.M.; Gautam G.; Bol'shakov, A.A; R. Russo. Molecular Laser-Induced Breakdown Spectroscopy, In *Laser Induced Breakdown Spectroscopy, 2nd Ed.*; J.P. Singh, S.N. Thakur, Eds.; Elsevier New York, Amsterdam, NL, 2020; Chap. 7, pp. 167–212.

[14] Parigger, C.G.; Hornkohl, J.O. *Quantum Mechanics of the Diatomic Molecule with* Applications; IOP Publishing: Bristol, UK, 2020.

[15] Parigger, C.G.; Woods, A.C.; Surmick, D.M.; Gautam, G.; Witte, M.J.; Hornkohl, J.O. *Spectrochim. Acta Part B At. Spectrosc.* 2015, *107*, 132–138.

[16] Parigger, C.G. *Spectrochim. Acta Part B At. Spectrosc.* 2021, *179*, 106122, 12 pp.

[17] Parigger, C.G.; Helstern, C.M; Jordan, B.S.; Surmick, D.M.; Splinter, R. *Molecules* 2020, *25*, 988, 18 pp.

[18] Parigger, C.G.; Helstern, C.M.; Jordan, B.S.; Surmick, D.M.; Splinter, R. *Molecules* 2020, *25*, 615, 13 pp.

[19] Gordon, S.; McBride, B. Computer program for calculation of complex equilibrium compositions, rocket performance, incident and reflected shocks, and Chapman-Jouguet detonations, NASA Lewis Research Center, Interim Revision, NASA Report SP-273 (1976).

[20] McBride, B.J.; S. Gordon. Computer Program for Calculating and Fitting Thermodynamic Functions, NASA RP-1271, 1992; on-line 2005 version, https://cearun.grc.nasa.gov/ (accessed December 14, 2019).

[21] Condon, E.U.; Shortley, G. *The Theory of Atomic Spectra*; Cambridge University Press: Cambridge, UK, 1953.